High-Resolution Photocurrent Microscopy Using Near-Field Cathodoluminescence of Quantum Dots

Heayoung P. Yoon[1,2]*, Youngmin Lee[1], Christopher D. Bohn[1], Seung-Hyeon Ko[1,2], Anthony G. Gianfrancesco[1,3], Jonathan S. Steckel[4], Seth Coe-Sullivan[4], A. Alec Talin[1,5], Nikolai B. Zhitenev[1]

[1]*Center for Nanoscale Science and Technology, National Institute of Standards and Technology, Gaithersburg, MD 20899, United States*

[2]*Maryland Nanocenter, University of Maryland, College Park, MD 20742, United States*

[3]*Department of physics, Worcester Polytechnic Institute, Worcester, MA 01602, United States*

[4]*QD Vision Inc., 29 Hartwell Ave., Lexington, MA 02421, United States*

[5]*Sandia National Laboratories, Livermore, CA 94550, United States*

Abstract

We report a fast, versatile photocurrent imaging technique to visualize the local photo response of solar energy devices and optoelectronics using near-field cathodoluminescence (CL) from a homogeneous quantum dot layer. This approach is quantitatively compared with direct measurements of high-resolution Electron Beam Induced Current (EBIC) using a thin film solar cell (*n*-CdS / *p*-CdTe). Qualitatively, the observed image contrast is similar, showing strong enhancement of the carrier collection efficiency at the *p-n* junction and near the grain boundaries. The spatial resolution of the new technique, termed Q-EBIC (EBIC using quantum dots), is determined by the absorption depth of photons. The results demonstrate a new method for high-resolution, sub-wavelength photocurrent imaging measurement relevant for a wide range of applications.

Scanning photocurrent microscopy permits monitoring carrier dynamics under an external excitation in real time, providing rich information on local electronic structures and optical properties in electronics and photonic devices. A laser beam induced current map has been used to investigate lateral inhomogeneity in a variety of semiconductor devices and solar cells, revealing the effect of local impurities and defects on the device performance[1][2]. Using a small fiber probe that can confine optical illumination below the diffraction limit[3], near-field optical scanning microscopy was used to spatially and spectrally resolve photo response of copper indium gallium disulfide (CIGS) solar cell with a lateral resolution of ≈200 nm[4]. The excess carriers (i.e., electron-hole pairs) in these methods are generated through local photon absorption. Alternatively, an electron beam (typically 1 keV to 30 keV) can directly create the carriers through an ionization process. High-throughput electron beam induced current (EBIC) measurements offer a spatial resolution as high as ≈20 nm both on the top surface and throughout the cross-section of the device, allowing *in-situ* measurement of the carrier dynamics at the level of individual micro/nanostructures[5][6][7]. However, the quantitative accuracy of EBIC mapping of low-energy carrier dynamics and thermalization processes may be compromised by the high-energy of the incident electrons. Additionally, direct electron irradiation can cause undesirable artifacts such as charging in poorly conducting materials and damage in organic, carbon-based (e.g., carbon nanotubes and graphene) and biological specimens[8][9].

High-energy electrons interact with a material by losing energy and exciting carriers (electrons and holes) and phonons. Some electrons are scattered back, leaving the sample surface after one or several elastic or inelastic collisions. The energy loss associated with the backscattered electrons depends on the atomic numbers or composition of the materials[10]. The remaining energy of the electron beam is deposited and dissipated in the sample, causing the

excitations of electrons and holes, generation of secondary electrons, characteristic X-rays, and photons (i.e., cathodoluminescence) as well as heat[11] [12]. Earlier experiments showed that the generation of one electron-hole pair corresponds to the loss of incident electron energy $\beta \times E_g$, where E_g is the energy band-gap of the material with $\beta \approx 3$ for many inorganic semiconductors and insulators[13] [14]. This empirical value, $\beta \approx 3$, accounts for all energy losses mentioned above as well as for energy relaxation of electrons and holes excited well above the band gap.

EBIC signal is generated when the electrons and holes are separated by an internal (or contact) electric field and extracted from the device, while cathodoluminescence (CL) is produced by the radiative recombination of the electron-hole pairs. Recently, CL of a silicon nitride film (ultraviolet photons) was used for optical imaging of latex spheres with a spatial resolution as high as ≈ 50 nm[15]. This attractive approach can be extended to *in-vivo* imaging of biological specimens in challenging environments (e.g., liquids)[16] [17]. In this Letter, we describe a fast, high-resolution photocurrent imaging technique, where a conformal quantum dot film efficiently converts a high energy electron beam into a localized photon source addressable by an electron beam. Q-EBIC (EBIC using quantum dots) results are compared to the corresponding EBIC data using a polycrystalline cadmium telluride (CdTe) solar cell. To assess the luminescence efficiency, CL spectra of quantum dots are compared to those of various semiconductors and phosphors.

Thin-film CdTe solar cells (≈ 1 cm $\times$ 2 cm) used in this work were extracted from a commercial solar module[7]. An Ohmic contact was made to *p*-CdTe either by using the metallization remaining on the surface after the extraction process or by evaporating Cu (2 nm) / Au (7 nm) metal contact. A nano-manipulator inside the scanning electron microscope (SEM)

with a tungsten probe (100 nm tip radius) wired to an EBIC preamplifier was placed on top of the contact to *p*-CdTe. The glass substrate coated with *n*-CdS (cadmium sulfide) / TCO (transparent conducting oxide) layer served as a common contact. To map the efficiency of the carrier collection throughout the entire *p-n* junction region, cross-sections (5 µm × 40 µm) of the device were prepared using a focused ion beam (FIB). Quantum dots (≈9 nm in diameter) served as CL phosphors, which were deposited as a conformal film on the rough surface of our CdTe solar cells. The homogeneous colloidal cadmium selenide / zinc cadmium sulfide (CdSe/ZnCdS) core/shell quantum dots in toluene showed an emission peak at ≈620 nm with a full width at half maximum (FWHM) of ≈30 nm as determined by either fluorescence spectroscopy or photoluminescence measurement[18]. A dip-coater was used for layer-by-layer assembly of the quantum dots on the CdTe solar cell. We used 0.001 mol/m^3 (0.1 M) 1, 3-propanedithiol (PDT) in acetonitrile solution as a cross-linking agent between the CdSe/ZnCdS quantum dot layers[19][20]. All dipping processes were carried out at a rate of 1 mm/s to give a fairly uniform final thickness of the CdSe/ZnCdS quantum dot layer of ≈50 nm, corresponding to ≈6 layers of quantum dots[18]. CL spectra were obtained using a Czerny-Turner spectrometer with a CCD (charged coupled device) camera, where the photons were collected by a diamond-tuned parabolic mirror and dispersed with a grating with a groove spacing of 150 mm^{-1} [21]. All measurements were performed at a chamber pressure of < 1.3×10^{-4} Pa (1×10^{-6} Torr) and the spot size of the electron beam was ≈2 nm. Figure 1 illustrates the schematic of the measurement approaches in this work, where the electron-hole pairs are created by the absorption of photons (Q-EBIC) or through an ionization process by electron beams (EBIC).

A field-emission SEM image shows a uniform coverage of CdSe/ZnCdS quantum dots on a thin metal contact to the CdTe absorber (Figure 2a). While the peak-to-valley surface

roughness of the CdTe (< 500 nm) is larger than the diameter of quantum dot (≈9 nm), the layer-by-layer assembly process provides a highly conformal coating over the large area. The film thickness (≈50 nm) is chosen to be sufficiently thick to absorb all incident electrons for a range of low acceleration voltages while thin enough to enable high-spatial resolution for photocurrent mapping. A set of measured current images of the CdTe solar cell was obtained on the same region for different acceleration voltages, as shown in Figure 2 (b-e). The bright contrast seen at many grain boundaries indicates higher carrier collection at grain boundaries than at grain interiors, consistent with our earlier work[7]. The contact metal (Cu/Au = 2nm/7nm) is sufficiently thick to serve as an electrical contact, but still thin enough to minimize the attenuation of injected electron absorption and photon emission from the CdTe absorber[22]. Because the penetration depth of the irradiated electron beam significantly increases with the acceleration voltage, the contribution of the EBIC to the total current becomes more significant than that of Q-EBIC (i.e., photons) at larger acceleration voltages.

Complementary CL spectra of the CdSe/ZnCdS QD coated CdTe specimen were collected at different acceleration voltages (Figure 2 f-i)[18], illustrating that at an electron energy of 5 keV and below, photon emission (≈620 nm) originated from the quantum dot layer (E_g = 2 eV). Only at higher energies do the electrons penetrate to the underlying CdTe (E_g = 1.5 eV) as evident by the emerging CL peak at ≈810 nm. We note here that quantitative comparison of the CL peak intensities (620 nm vs. 810 nm) is not straightforward. First, the light extraction can be significantly different. Considering photon generation from an incoherent, unpolarized point source and taking the refractive index of CdSe/ZnCdS and CdTe to be 1.7 and 2.9, respectively, the estimated fraction of the photons emitted to vacuum through a planar interface is ≈8.4 % and ≈2 %[23]. Finite-difference time-domain (FDTD) simulations suggest that the fractions increase to

≈16 % for the QD layer and ≈2 % for CdTe when light reflection off a back Cu/Au metal layer is considered[18]. Second, electric fields in the n-CdS/p-CdTe solar cell separate electrons and holes, reducing the corresponding CL intensity at 810 nm. In an ideal solar cell, where the generated electron-hole pairs are separated and collected without any recombination, the CL intensity should vanish. A detailed discussion of CL intensity is provided later in this paper. Nevertheless, the peak of CdTe dominates over the quantum dot emission (Figure 2 h, i) with further increase in the electron beam voltage, as the fraction of the total energy deposition in the quantum dot layer diminishes. These results strongly suggest that the obtained Q-EBIC images at low accelerating voltage (< 6 keV) are primarily the result of CL photons emitted from the CdSe/ZnCdS quantum dots rather than the direct electron beam excitation of CdTe. In addition, Monte-Carlo simulations of the electron beam absorption in the QD layer support this conclusion (Figure 3b; discussed below).

To further investigate the distinct local photo response of Q-EBIC in comparison to corresponding EBIC, a systematic study was performed using a FIB cross-sectioned CdTe solar cell. The FIB process results in a smoother surface than the native top surface, thus minimizing possible effects of surface roughness[7] on light or electron beam injection. An SEM image of a CdS/CdTe cross-section covered with the CdSe/ZnCdS quantum dots (≈50 nm thick layer) for Q-EBIC measurements is shown in Figure 3a. We performed Monte Carlo simulations[24] to estimate the effective size of the light source and the best possible spatial resolution in Q-EBIC (Figure 3b, 3d). Assuming close-packed CdSe/ZnCdS quantum dots[18], the estimated range of electron beam absorption extends ≈55 nm at 3 keV (Figure 3b). However, over 75 % of the electron energy is absorbed within ≈25 nm thick of the CdSe/ZnCdS quantum dot layer, creating

a local photon source. For comparison, Figure 3d shows a simulation result of the 3 keV electron beam incident into a bare CdTe layer.

Figure 4 shows a direct comparison between Q-EBIC (Figure 4, a-f) and EBIC (Figure 4, g-l) images at different accelerating beam voltages. Overall, the Q-EBIC and EBIC images are quite similar. In both cases, a higher current was observed near the *p-n* junction, where the internal electric field separates the generated electron-hole pairs. The magnitude of the maximum current increases at larger electron beam voltages in both Q-EBIC and EBIC images. At a high excitation voltage (e.g., 15 keV), the magnitude of the current becomes similar as a consequence of a deep injection of the electron beam. However, a careful inspection of the current distribution of the images indicates a lower spatial resolution in the Q-EBIC than in EBIC at lower accelerating voltage (3 keV), as evident in the vicinity of grain boundaries. Unlike the EBIC, where the electron-hole pairs are generated within the generation bulb determined by the electron beam energy (e.g., ≈20 nm at 3 keV in CdTe), the spatial resolution of the Q-EBIC is determined both by the excitation bulb and by the absorption depth of the photons emitted from the quantum dot layer. Photons with a wavelength of 620 nm travel ≈150 nm in CdTe before the original intensity drops by a factor of 1/e (67 %)[25], corresponding to the penetration depth of the electron beam at 7 keV (estimated by a Monte Carlo simulation[24]). Thus, the resolution of Q-EBIC image collected at 3 keV parallels the EBIC images collected at 7 keV but a different magnitude of current (i.e., larger number of carrier generation with 7 keV). This limitation of practical resolution in the current experiment also suggests that a possible thickness variation of the QD film will not affect the image if the film thickness is in the range from 20 nm (excitation bulb at 3 keV) to 150 nm (absorption depth of CdTe at 620 nm).

The maximum current measured with Q-EBIC (22 nA) at 3 keV is higher than the current measured with EBIC (17 nA) at the same accelerating voltage. This is perhaps surprising; the band-gap of the quantum dots is greater (E_g = 2 eV) than CdTe (E_g = 1.5 eV), implying less electron-hole pairs created in CdSe/ZnCdS compared to CdTe for a fixed electron beam voltage. The fact that the external quantum efficiency is nevertheless greater for Q-EBIC is reflective of two factors: (1) very efficient photon generation in the CdSe/ZnCdS layer, and (2) Enhanced efficiency of charge collection when carriers are excited by photons emitted by the quantum dots, compared to the excitation by electrons. The latter can be understood as a consequence of the increased absorption depth of photons compared to electrons: generating electron-hole pairs deeper in the interior of the CdTe minimizes surface recombination.

We estimate the internal quantum efficiency of the quantum dot using the measured current $\left(I_{Q-EBIC}\right)$ in the Q-EBIC experiment. The CL IQE $\left(IQE_{CL;QD}\right)$ is defined by the number of photons divided by the number of excited electron-hole pairs.

$$I_{Q-EBIC} = \left(r_{ehp,\,QD}\right)\left(IQE_{CL;QD}\right)\left(f_{CL;\,QD \rightarrow CdTe}\right)\left(IQE_{CdTe}\right)$$

, where $r_{ehp,\,QD}$ is the generation rate of electron-hole pairs in quantum dot layer and $f_{CL;\,QD \rightarrow CdTe}$ is the fraction of photon emission from the quantum dot layer to CdTe. For the collection efficiency of CdTe $\left(IQE_{CdTe}\right)$ we use the measured EBIC data. To ensure similar collection efficiency and, respectively, the absorption depth as described above, we compare 3 keV Q-EBIC and 7 keV EBIC data, where the electron-hole pairs were generated within the same volume of the CdTe absorber (i.e., same average extraction efficiency of electrons and holes). A 7 keV electron injected in the CdTe absorber (E_g = 1.5 eV) creates ≈1150 electron-hole pairs by

assuming that $3 \times E_g$ electron beam energy is necessary to generate one electron-hole pair[13] and accounting for the calculated backscattered energy loss of $\approx$26 % [26]. This equals to the maximum current of $\approx$440 nA under the electron beam current of $\approx$380 pA. The observed maximum current at 7 keV in EBIC is $\approx$110 nA, resulting in collection efficiency for CdTe $\left(IQE_{CdTe} \right)$ of $\approx$25 %. The estimated fraction of photon emission from the quantum dot to the CdTe layer $\left(f_{CL; QD \rightarrow CdTe} \right)$ is $\approx$90%. This is due to the difference of the refractive indices of the CdTe ($n = 2.9$), the quantum dot layer ($n = 1.7$), and the vacuum ($n = 1$)[18]. The generation rate of electron-hole pairs in the quantum dots $\left(r_{ehp, QD} \right)$ can again be estimated from the band-gap and the deposited electron beam energy: a 3 keV electron in the CdSe/ZnCdS quantum dot ($E_g = 2$ eV) layer creates $\approx$390 electron-hole pairs, suggesting the maximum photocurrent of $\approx$100 nA at a beam current of $\approx$260 pA. With these estimates, and the measured current of 22 nA, we find the cathodoluminescence IQE of the quantum dots $\left(IQE_{CL;QD} \right)$ is close to $\approx$100 %. Such high efficiency has been demonstrated for photoluminescence through multiple exciton generation[19,27,28], yet it has been rarely reported for cathodoluminescence of quantum dots. The accuracy of this evaluation is limited by strong local variations of the electron-hole collection efficiency in the CdTe solar cell.

To independently and reliably measure the internal quantum efficiency of CL, we extensively compare the CL characteristics of the CdSe/ZnCdS quantum dot film with bulk semiconductors, commercial phosphor, and commercial quantum dots[18]. As direct band-gap semiconductors, high purity GaAs ($E_g = 1.45$ eV) and InP ($E_g = 1.35$ eV) single crystalline materials have shown high internal quantum efficiencies over 90 % [29,30,31]. For this comparison, we prepared a thick film (> 1 μm) of CdSe/ZnCdS quantum dots by drop-casting onto a bare Si substrate. All spectra were obtained by integrating the CL signal for 1 s, where the entrance slit

of the spectrometer was fully open. Figure 5 (a) displays the measured CL spectra at 10 keV. The characteristic peaks at 620 nm for QD, 850 nm for GaAs, and 920 nm for InP are matching to their corresponding band-gaps, but the CL intensity of CdSe/ZnCdS QD film is much higher than those of GaAs and InP. This high CL intensity of the QD was observed at different acceleration voltages as shown in the inset to Figure 5 (b). The count represents the collected total number of CL photons extracted from each spectrum. Due to the refractive indices of the QD film ($n = 1.9$), InP ($n = 3.3$), and GaAs ($n = 3.7$) at the emission wavelengths (measured by spectroscopic ellipsometery), the fraction of the escaping photons from the materials to the vacuum is different. The estimated CL fraction is 7 % for QD film, 1.7 % for InP, and 1.2 % for GaAs[23]. The estimated backscattered energy loss is ≈28 % for the QD film, ≈27 % for InP, and ≈22 % for GaAs from the Monte Carlo simulations. Figure 5 (b) compares the normalized CL signals accounting for the difference in the emission cone (CL fraction), the backscattered energy loss, and the number of generated CL photons. Assuming that IQE is close to 100 % in the high purity GaAs or InP, we calculate IQE of QD film as 102 ± 7 %[18]. This value is consistent with the IQE value determined in the Q-EBIC measurements.

In summary, we presented a new photocurrent imaging approach that combines the high speed and versatility of electron microscopy with optical microscopy by down-converting high energy electrons to local photons through CL in quantum dots. The near-field CL of the CdSe/ZnCdS quantum dot layer is very bright, and the generated photocurrent exceeds the direct EBIC signal within a useable range of parameters. Beyond the immediate application to the local characterization of various types of solar cells and optoelectronic devices, the approach has general advantages for a broad range of microscopies. Sample under study is not exposed to direct electron beam irradiation as the incident beam is fully absorbed in the quantum dots layer
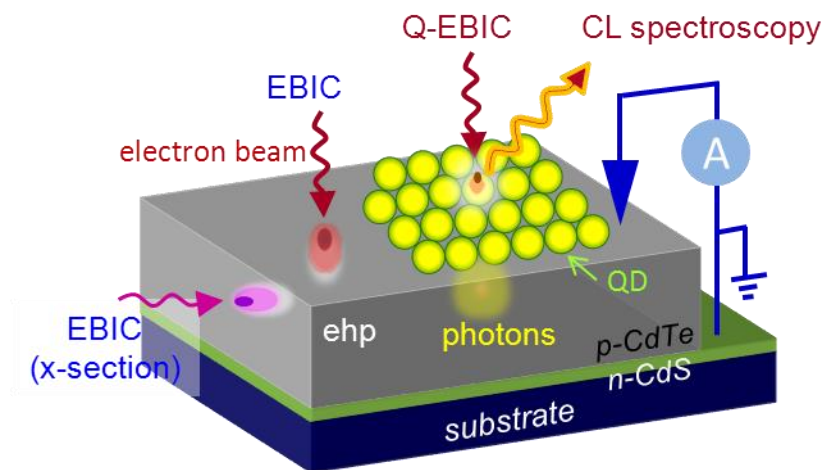
conforming to the sample surface. Compared to near-field optical scanning microscopy or other super-resolution optical microscopies, the current approach is high-throughput, can be used for samples with rough surface topography and features the high depth of focus typical for electron microscopy.
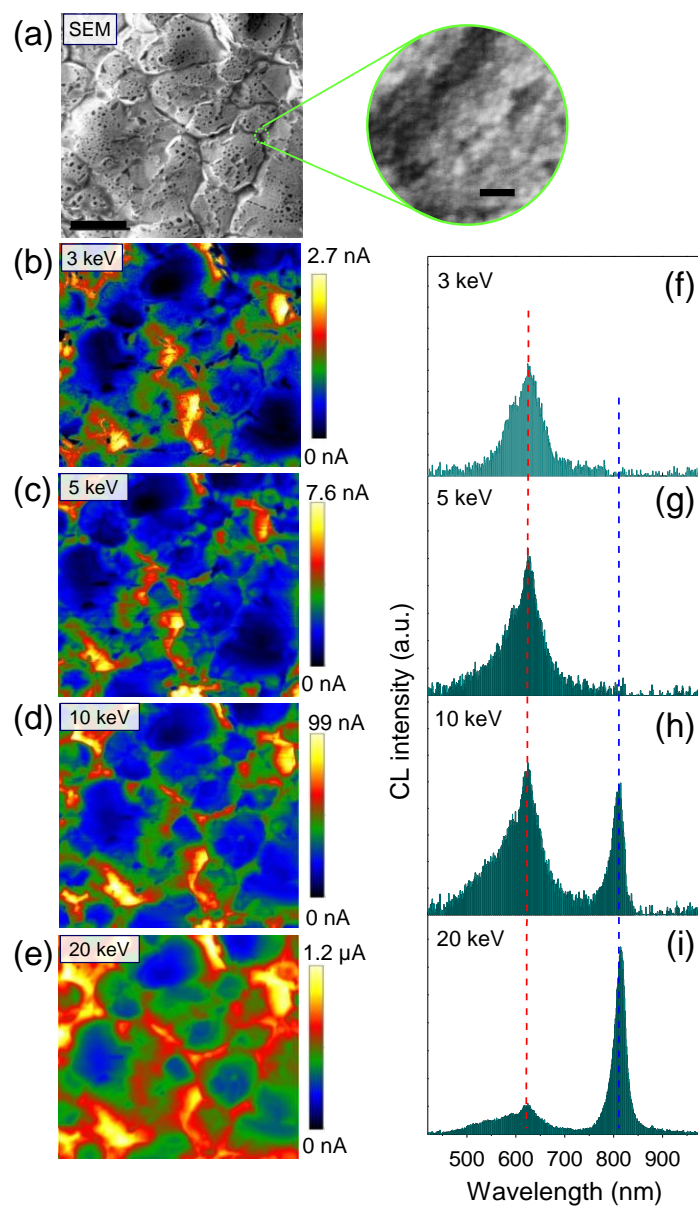
Acknowledgement

Figure 1.

Schematic of Q-EBIC (EBIC using quantum dots), EBIC (electron beam induced current), and cathodoluminescence (CL) measurements that are made on a CdTe solar cell. An irradiated electron beam on the quantum dots generates photons through the recombination of electron-hole pairs (ehp). The emitted photons are absorbed in the CdTe, producing a local current (Q-EBIC). In contrast, EBIC collects electron-hole pairs that are directly generated through an ionization process in the CdTe. CL spectroscopy collects the fraction of the photons that are emitted into vacuum.
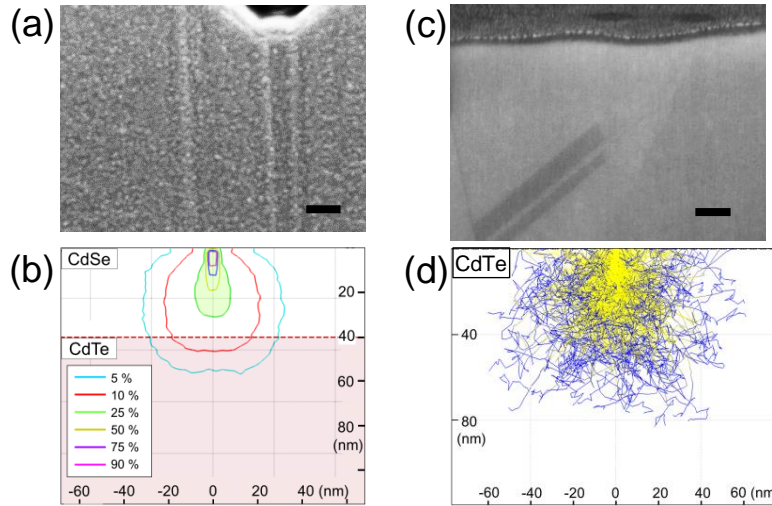
Figure 2.

(a) SEM image of a CdSe/ZnCdS quantum dot layer assembled on a *p*-CdTe / *n*-CdS solar cell (scale bar 1 μm). Inset shows the high magnification of the conformal assembly of the quantum dot (scale bar 50 nm). Q-EBIC images (b-e) and the corresponding CL spectra (f-i) as a function of electron beam voltage (3 keV, 5 keV, 10 keV, and 20 keV), respectively. The bright contrast seen at many grain boundaries indicates higher excess carrier collection as compared to grain interiors. The prominent peaks at 620 nm (red line) and 810 nm (blue line) arise from band-to-band radiative recombination in the CdSe/ZnCdS quantum dot (E_g = 2 eV) and the CdTe absorber (E_g = 1.5 eV), respectively. The FWHM of the assembled quantum dot layer is broader (≈70 nm) than in the photoluminescence (≈30 nm) measurement, likely due to the cross-linking molecules (1, 3-propanedithiol).

(a) SEM

(b) 3 keV — 2.7 nA / 0 nA

(c) 5 keV — 7.6 nA / 0 nA

(d) 10 keV — 99 nA / 0 nA

(e) 20 keV — 1.2 µA / 0 nA

(f) 3 keV

(g) 5 keV

(h) 10 keV

(i) 20 keV

CL intensity (a.u.)
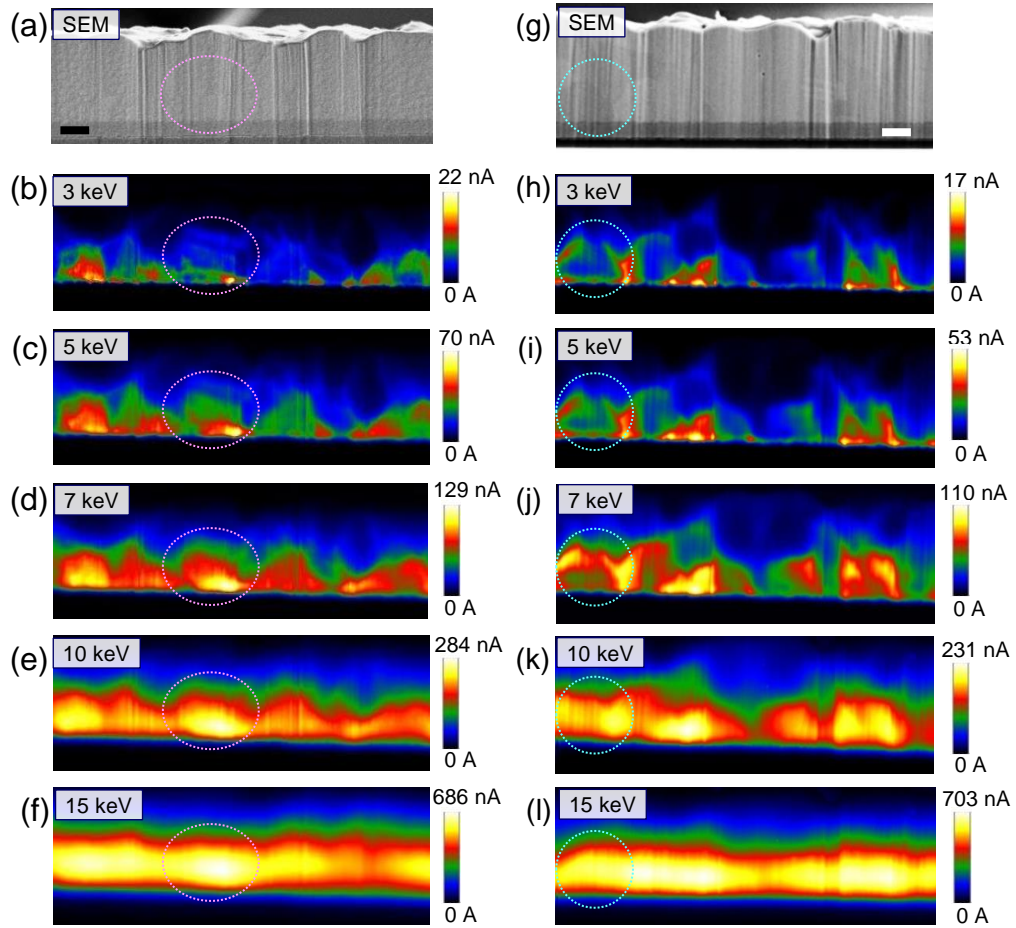
Wavelength (nm)

500 600 700 800 900

Figure 3.

Cross-sectional SEM images of CdTe absorber with a layer of CdSe/ZnCdS quantum dots (a) and a bare surface (c). (b) A Monte-Carlo simulation shows the range of carrier generation extends ≈55 nm at a 3 keV electron beam irradiation in a 40 nm thick CdSe layer. We assumed a close-packing of the CdSe/ZnCdS core/shell quantum dots (≈9 nm in diameter) in the ≈50 nm thick layer, estimating an equivalent film of 40 nm thick CdSe. The thicknesses of the QD ligand and the cross-linking molecules (≈0.6 nm)[32] were not counted. The legend numbers show the percentage of energy deposited outside of the corresponding contour lines. Over 75 % of the electron energy is deposited within a volume of ≈25 nm in diameter (green area). (d) Simulation of 3 keV electron beam irradiation of a bare CdTe layer. The penetration depth is comparable to that of CdSe/ZnCdS. The energy of the electrons is color coded from yellow (high energy) to blue (low energy).
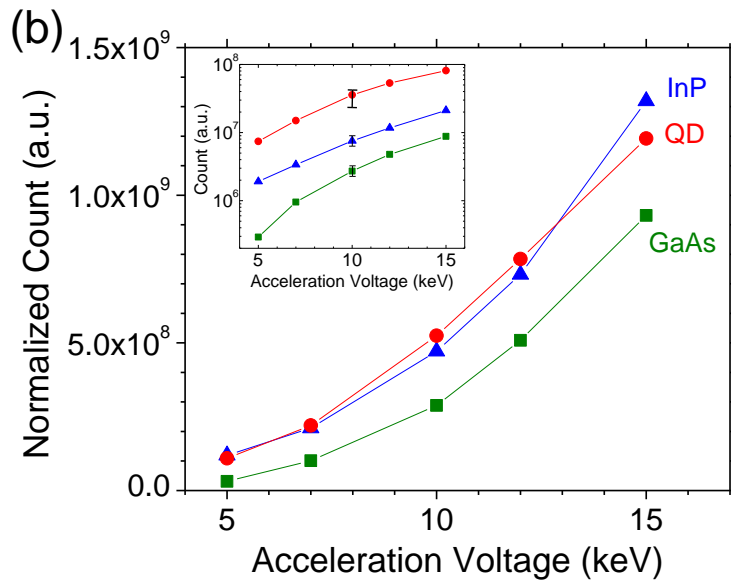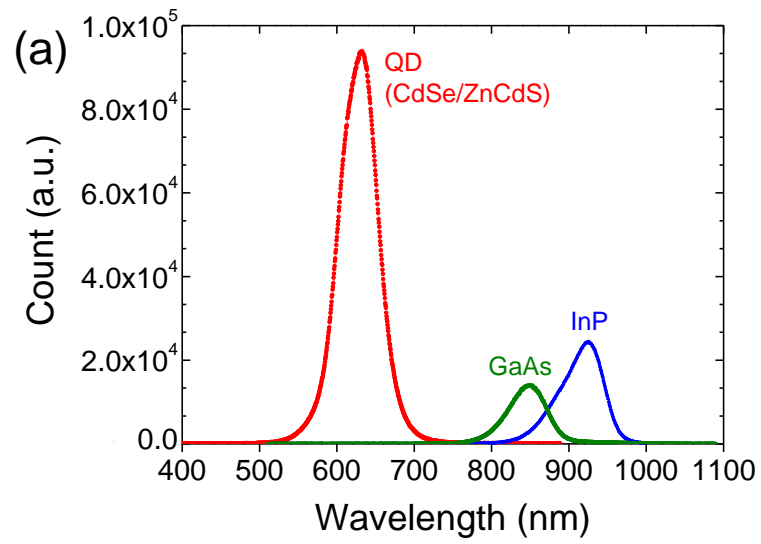
Figure 4.

Cross-sectional SEM images of *n*-CdS / *p*-CdTe solar cell with (a) and without (g) an assembly of CdSe/ZnCdS quantum dots. A series of corresponding Q-EBIC (b-f) and EBIC (h-l) images at different electron beam voltages. The top value of each scale bar represents an average of the 50 highest pixel currents in the 1024 × 1024 current map (electron beam step size ≈16 nm). The circle in the images identifies a single grain in the CdTe absorber. Uncertainty of the values in the scale bars is ≈8% (one standard deviation) due to strong local variation of the electron-hole collection efficiency in the CdTe solar cell. (Scale bar: 1 µm)

Figure 5.

(a) 10 keV CL spectra of CdSe/ZnCdS quantum dot film and GaAs and InP single crystalline materials. The characteristic peaks at 620 nm for QD, 850 nm for GaAs, and 920 nm for InP correspond to the band-edge recombination. (b) Inset shows the integrated number of collected photons at different acceleration voltages. The counts are normalized to account for the escape fraction of CL for each material $\left(f_{QD} = 7\%, f_{InP} = 1.7\%, f_{GaAs} = 1.2\% \right)$, the backscattered electron energy loss (28 % for QD film, 27 % for InP, 22 % for GaAs), and the number of generated CL photons. Representative error bars indicate one standard deviation uncertainties due to the spectroscopic collection setup and background signal of the CCD (charged coupled device) detector.

References

1.	J. Marek, J Appl Phys 55 (2), 318-326 (1984).
2.	J. Carstensen, G. Popkirov, J. Bahr and H. Foll, Sol Energ Mat Sol C 76 (4), 599-611 (2003).
3.	S. Smith, P. Zhang, T. Gessert and A. Mascarenhas, Appl Phys Lett 85 (17), 3854-3856 (2004).
4.	J. K. Larsen, L. Gutay, Y. Aida and S. Siebentritt, Thin Solid Films 519 (21), 7332-7336 (2011).
5.	P. R. Edwards, S. A. Galloway and K. Durose, Thin Solid Films 372 (1-2), 284-291 (2000).
6.	C. Gutsche, R. Niepelt, M. Gnauck, A. Lysov, W. Prost, C. Ronning and F. J. Tegude, Nano Lett 12 (3), 1453-1458 (2012).
7.	H. P. Yoon, D. Ruzmetov, P. M. Haney, M. S. Leite, B. H. Hamadani, A. A. Talin and N. B. Zhitenev, 38th IEEE PVSC, 3217-3219 (2012).
8.	P. Reuter, T. Rath, A. Fischereder, G. Trimmel and P. Hadley, Scanning 33 (1), 1-6 (2011).
9.	M. Sezen, H. Plank, P. M. Nellen, S. Meier, B. Chernev, W. Grogger, E. Fisslthaler, E. J. W. List, U. Scherf and P. Poelt, Phys Chem Chem Phys 11 (25), 5130-5133 (2009).
10.	C. A. Klein, IEEE J Quantum Elect QE-4 (4), 186-194 (1968).
11.	L. Reimer, Scanning electron microscopy: physics of image formation and microanalysis, (Springer, 1998).
12.	F. J. G. de Abajo, Rev Mod Phys 82 (1), 209-275 (2010).
13.	C. A. Klein, J Appl Phys 39 (4), 2029 (1968).
14.	H. J. Leamy, J Appl Phys 53 (6), R51-R80 (1982).
15.	W. Inami, K. Nakajima, A. Miyakawa and Y. Kawata, Opt Express 18 (12), 12897-12902 (2010).
16.	N. de Jonge and F. M. Ross, Nat Nanotechnol 6 (11), 695-704 (2011).
17.	Y. Nawa, W. Inami, A. Chiba, A. Ono, A. Miyakawa, Y. Kawata, S. Lin and S. Terakawa, Opt Express 20 (5), 5629-5635 (2012).
18.	See supplementary material at [AIP] for fluorescence and photoluminescence spectra, size of the QDs and the thickness of the QD layer, a set of CL spectra at different acceleration voltages, details of analytical and FDTD calculations, estimated CL fractions, and for more comparison.
19.	O. E. Semonin, J. M. Luther, S. Choi, H. Y. Chen, J. B. Gao, A. J. Nozik and M. C. Beard, Science 334 (6062), 1530-1533 (2011).
20.	M. Law, M. C. Beard, S. Choi, J. M. Luther, M. C. Hanna and A. J. Nozik, Nano Lett 8 (11), 3904-3910 (2008).
21.	P. Das and T. K. Chini, Curr Sci India 101 (7), 849-854 (2011).

22. H. Klauk, J. R. Huang, J. A. Nichols and T. N. Jackson, Thin Solid Films 366 (1-2), 272-278 (2000).

23. P. W. Hawkes, Advances in imaging and electron physics (Academic Press, San Diego, 2007).

24. D. Drouin, A. R. Couture, D. Joly, X. Tastet, V. Aimez and R. Gauvin, Scanning 29 (3), 92-101 (2007).

25. K. Mitchell, A. L. Fahrenbruch and R. H. Bube, J Appl Phys 48 (2), 829-830 (1977).

26. I. H. Campbell and B. K. Crone, Adv Mater 18 (1), 77-79 (2006).

27. R. J. Ellingson, M. C. Beard, J. C. Johnson, P. R. Yu, O. I. Micic, A. J. Nozik, A. Shabaev and A. L. Efros, Nano Lett 5 (5), 865-871 (2005).

28. Z. T. Kang, Y. L. Zhang, H. Menkara, B. K. Wagner, C. J. Summers, W. Lawrence and V. Nagarkar, Appl Phys Lett 98 (18) (2011).

29. B. G. Yacobi and D. B. Holt, J Appl Phys 59 (4), R1-R24 (1986).

30. J. J. Zou, B. K. Chang, H. L. Chen and L. Liu, J Appl Phys 101 (3) (2007).

31. M. Inoue, J Appl Phys 55 (6), 1558-1565 (1984).

32. M. D. Porter, T. B. Bright, D. L. Allara and C. E. D. Chidsey, J Am Chem Soc 109 (12), 3559-3568 (1987).

[Supporting Information]

High-Resolution Photocurrent Microscopy Using Near-Field Cathodoluminescence of Quantum Dots

Heayoung P. Yoon[1,2]*, Youngmin Lee[1], Christopher D. Bohn[1], Seung-Hyeon Ko[1,2], Anthony G. Gianfrancesco[1,3], Jonathan S. Steckel[4], Seth Coe-Sullivan[4], A. Alec Talin[1,5], Nikolai B. Zhitenev[1]

[1]Center for Nanoscale Science and Technology, National Institute of Standards and Technology, Gaithersburg, MD 20899, United States

[2]Maryland Nanocenter, University of Maryland, College Park, MD 20742, United States

[3]Department of physics, Worcester Polytechnic Institute, Worcester, MA 01602, United States

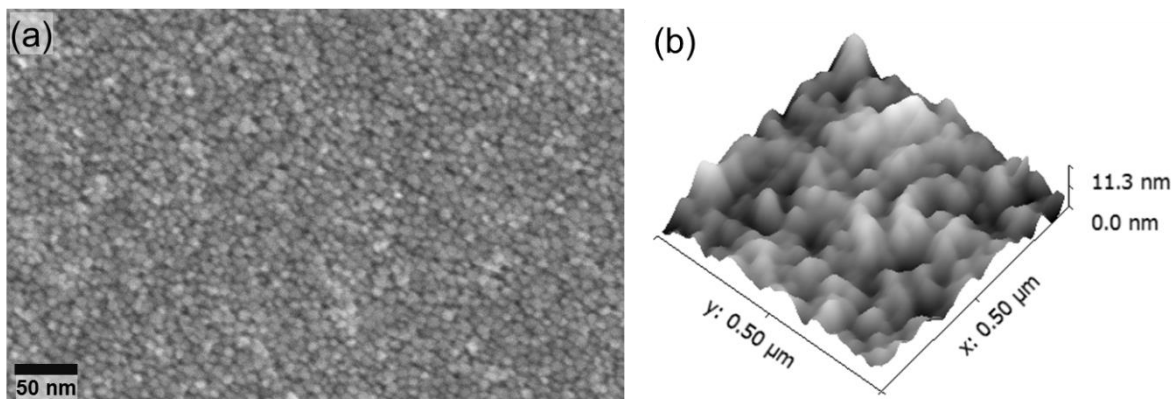[4]QD Vision Inc., 29 Hartwell Ave., Lexington, MA 02421, United States

[5]Sandia National Laboratories, Livermore, CA 94550, United States
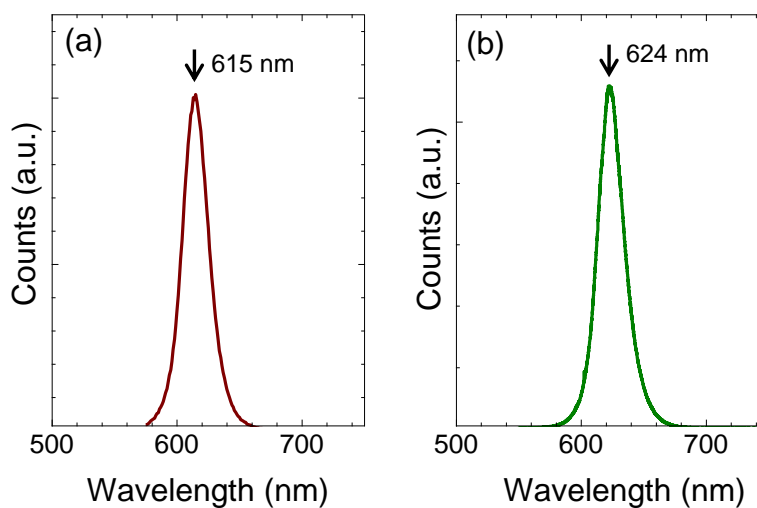
1. Quantum dot assembly

A conformal quantum dot (QD) layer was assembled on a cadmium telluride (CdTe) solar cell (n-CdS / p-CdTe) using a dip coater. For planar Q-EBIC (electron beam induced current using QDs) measurements, the cadmium selenide / zinc cadmium sulfide (CdSe/ZnCdS) core/shell quantum dots were deposited on the evaporated Cu/Au (2 nm/7 nm) contact metal on the CdTe absorber. The sample was dipped into 0.001 mol/m^3 (0.1 M) of 1,3-propanedithiol (PDT) in acetonitrile and was pulled out at the speed of 1mm/s. Following a rinse in acetonitrile to eliminate unbound thiol, the substrate was dipped in the CdSe/ZnCdS QD solution (5.83 mg/ml). The process was repeated three times, resulting in a final thickness of ≈50 nm (≈6 QD layers). For cross-sectional Q-EBIC measurements, the CdTe solar cell sectioned by the focused ion beam (FIB) was immersed in 2 mM of hexadecanethiol in ethanol solution for 8 hours to prepare a hydrophobic surface prior to the QD assembly. After rinsing the substrate in ethanol and blow-drying with N_2, the substrate was attached to the dip-coater. The sample was dipped into the CdSe/ZnCdS QD solution following the same assembly conditions above. Figure S-1 shows an SEM (scanning electron microscopy; a) image and an AFM (atomic force microscopy; b) image of the QD layer assembled on a control sample (7 nm Au / 2nm Cu / Si wafer) after the three dipping sequences.
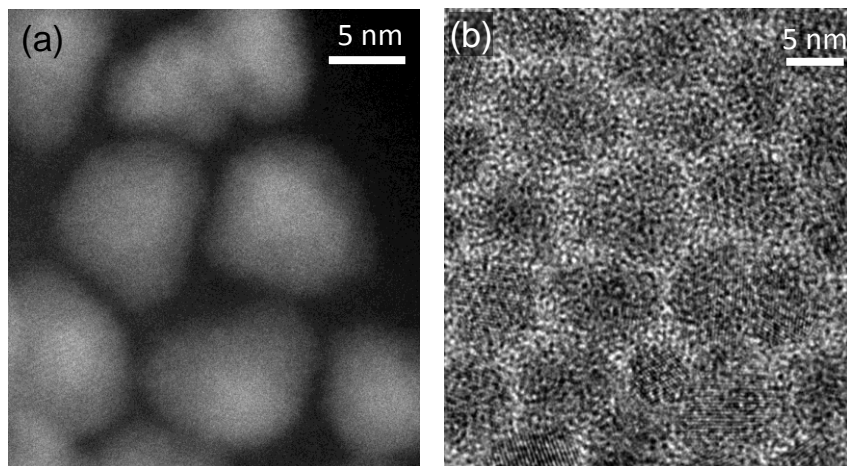
Figure S-1. Representative SEM (a) and 3D AFM (b) images of a highly-packed CdSe/ZnCdS

QD layer. The root-mean-square surface roughness is ≈1.3 nm.
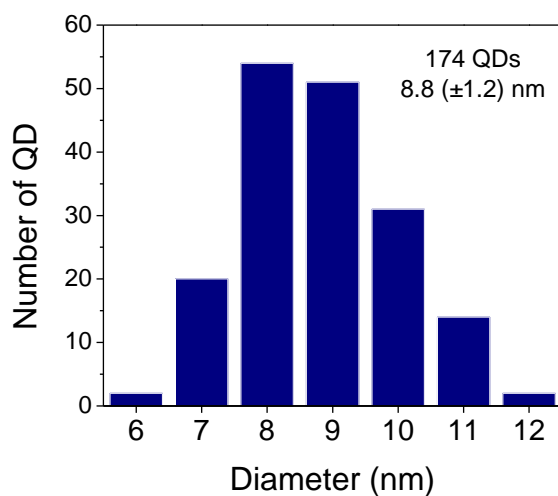
2. Photoluminescence / fluorescence measurements

Figure S-2. (a) Fluorescence spectrum of the colloidal CdSe/ZnCdS QDs used in this work

showed an intense peak at ≈615 nm. (b) A drop of the CdSe/ZnCdS QD solution was deposited

on a glass substrate and dried for photoluminescence spectroscopy. Full width at half maximum

of the peak is ≈30 nm for both cases.
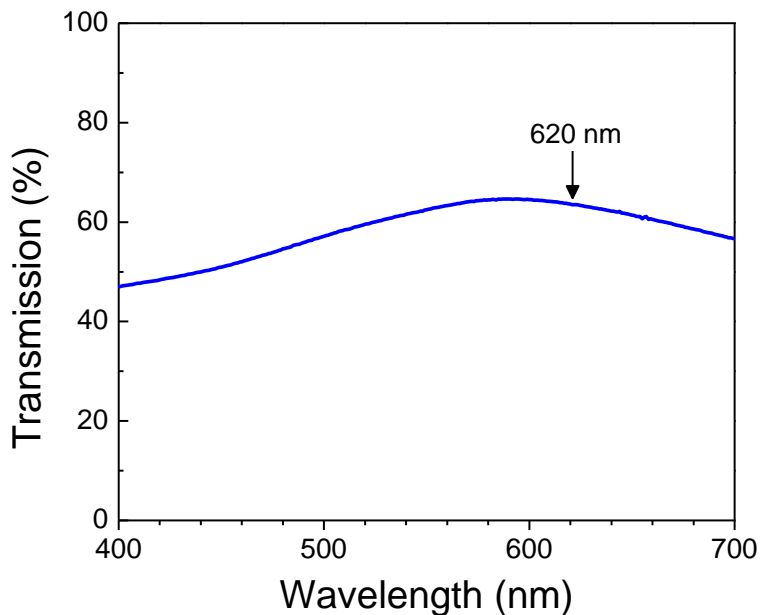
3. Size of CdSe/ZnCdS quantum dots

Figure S-3. CdSe/ZnCdS QDs in toluene were transferred to hexane, and a drop of the diluted QD solution was deposited on an amorphous carbon coated Cu grid under ambient conditions. Scanning transmission electron microscope image (STEM; a) and TEM image (b) were obtained at an acceleration voltage of 300kV.
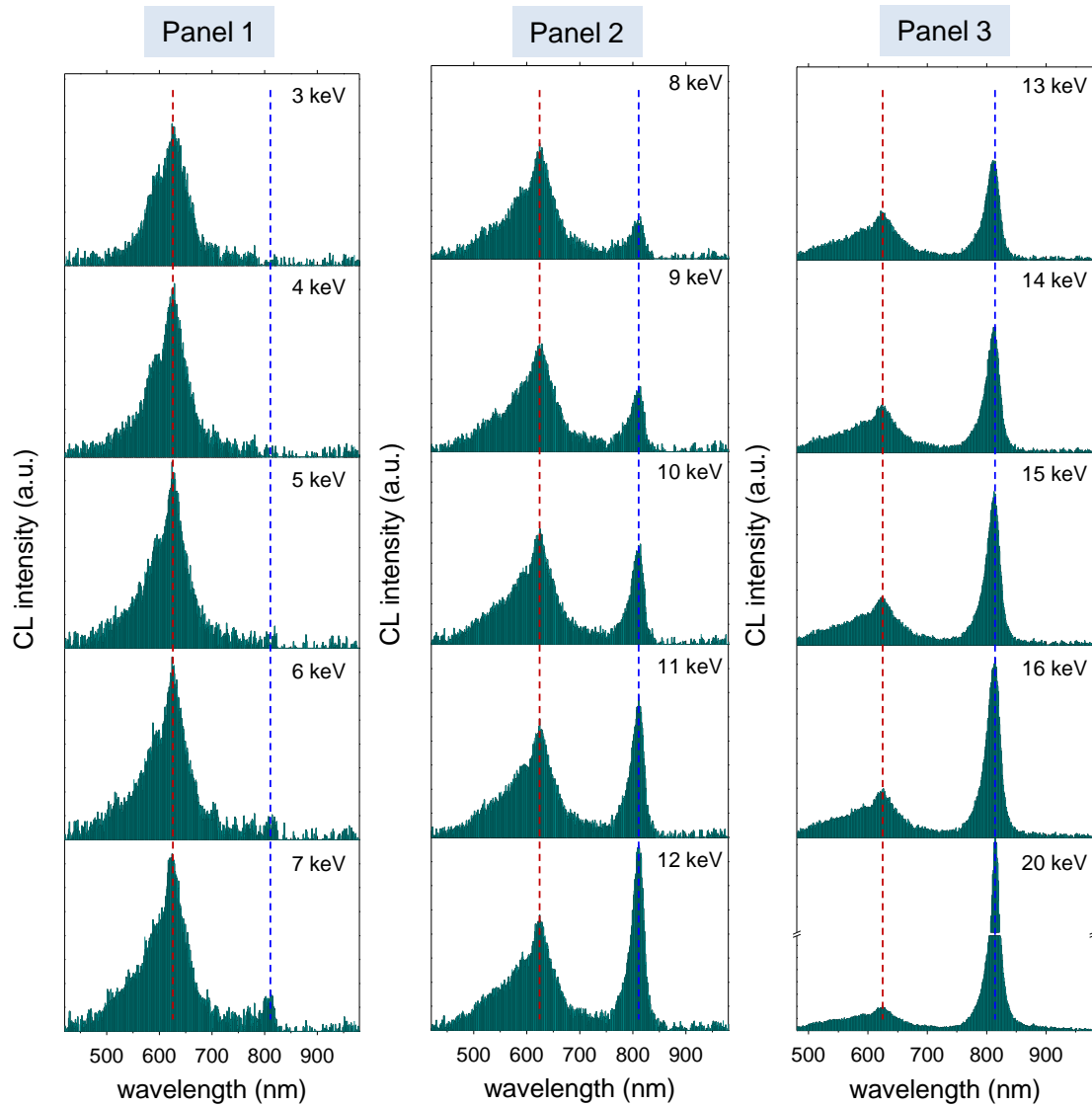

Figure S-4. The average diameter of the CdSe/ZnCdS QDs is 8.8 ($\pm$1.2) nm based on measurements of 174 QDs. Assuming a close-packing of spheres (filling fraction of $\approx$74 %), we estimated $\approx$6 layers of QDs in $\approx$50 nm thick CdSe/ZnCdS QD layer.

4. CL spectra of CdSe/ZnCdS QD film assembled on CdTe solar cell

A set of CL spectra was collected on the CdSe/ZnCdS QD coated CdTe solar cell at different acceleration voltages. The contact metal on the CdTe absorber (Cu/Au = 2nm/7nm) is sufficiently thick to serve as an electrical contact, but still thin enough to insignificantly attenuate the electron beam injection into the CdTe layer or the emission of the photons generated in the CdTe absorber layer. The observed CL spectra in Figure S-6 suggested that at the electron energy of 5 keV and below, photon emission ($\approx$ 620 nm) originated from the quantum dot layer. Although the estimated fraction of CL emission (Equation S-4) from the CdSe/ZnCdS QD layer ($\approx$16 %) is larger than that of CdTe absorber ($\approx$2 %), the integrated photon counts from to the CdSe/ZnCdS QD layer at 620 nm ($\approx$ 1800 at the peak) is much higher than that from the CdTe at 810 nm ($\approx$ 100 at the peak).

Figure S-5. A representative transmittance spectrum of a thin metal film (Cu/Au = 2 nm/7 nm) deposited on a slide glass. The transmittance at 620 nm (arrow) is 65 ± 5 %.

Figure S-6. A set of CL spectra of a CdSe/ZnCdS QD on top of CdTe specimen collected at different acceleration voltages. The prominent peaks at ≈620 nm (red line) and ≈810 nm (blue line) arise from band-to-band radiative recombination in the CdSe/ZnCdS quantum dot (E_g = 2 eV) and the CdTe absorber (E_g = 1.5 eV), respectively. The maximum counts (y-axis) is 1800 in panel 1, 3000 in panel 2, and 7000 in panel 3 (11000 for 20 keV).

5. Fraction of CL emission

The fraction of cathodoluminescence $\left(f_{CL}\right)$ depends on the refractive index of the materials. Light transmission (T) at an interface is determined from the Fresnel equations.

$$T \approx 1 - \left(\frac{n_1 - n_2}{n_1 + n_2}\right)^2 \tag{S-1}$$

From Snell's law, light is transmitted from a medium_2 with a refractive index $\left(n_2\right)$ to a medium_1 $\left(n_1\right)$ when the illumination angle is below a critical value,

$$\phi_c = \sin^{-1}\left(\frac{n_1}{n_2}\right) \text{ and } n_2 > n_1. \tag{S-2}$$

Integrating the fractional area of a sphere (radius of R) with $\phi < \phi_c$ gives:

$$\frac{\int_0^{2\pi}\int_0^{\phi_c} R^2 \sin(\phi)\, d\phi\, d\theta}{4\pi R^2} = \frac{[1 - \cos(\phi_c)]}{2} = \frac{1}{2}\left[1 - \sqrt{1 - \left(\frac{n_1}{n_2}\right)^2}\right] \tag{S-3}$$

Thus, the total fraction of light transmitted from an incoherent, unpolarized point source incident on a planar interface (Figure S-7 a) is then approximated by combining the results from equations (S-1) and (S-3) through multiplication.
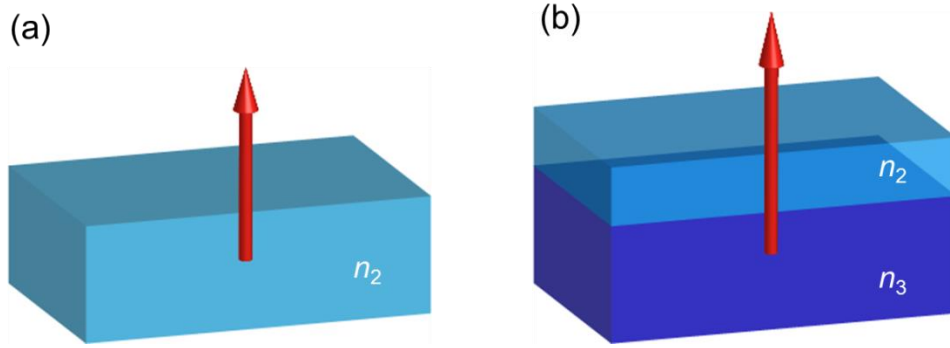
$$f_{CL} \approx \frac{1}{2}\left[1 - \left(\frac{n_1 - n_2}{n_1 + n_2}\right)^2\right]\left[1 - \sqrt{1 - \left(\frac{n_1}{n_2}\right)^2}\right] \tag{S-4}$$

Using this equation, the estimated CL fractions for CdTe ($n = 2.9$), CdS ($n = 2.4$), InP ($n = 3.3$), and GaAs ($n = 3.7$) bulk materials emitting to vacuum are 8.9 %, 3.8 %, 1.7 %, and 1.2 %, respectively. We note here that the CL fraction (f_{CL}) is sensitive to the value of refractive index.

In the case of a stacked structure (Figure S-7 b), where the top layer is relatively transparent (i.e., insignificant internal reflectance), the CL fraction from the medium_3 to medium_1 through medium_2 can be written as:

$$f_{CL2} \approx \frac{1}{2}\left[1-\left(\frac{n_1-n_2}{n_1+n_2}\right)^2\right]\left[1-\left(\frac{n_2-n_3}{n_2+n_3}\right)^2\right]\left[1-\sqrt{1-\left(\frac{n_1}{n_3}\right)^2}\right] \tag{S-5}$$

Using equation (S-5), we estimate the CL fraction from the CdTe ($n = 2.9$) covered with a thin layer of CdSe/ZnCdS QD layer ($n = 1.7$) to be 0.03.
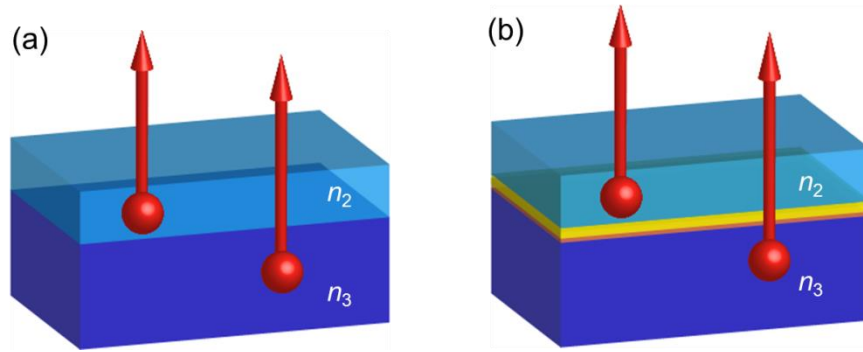

Figure S-7. Fractional CL emission to vacuum from an incoherent, unpolarized point source in bulk (a; GaAs, InP, CdS) and stacked layers (b; CdSe/ZnCdS QD layer on CdTe)

The analytical calculations do not take into account interference effects which arise in thin films. While these numbers represent a good approximation for a thick sample (thickness $\gg$ wavelength of CL), they will not be accurate for a thin film. For such cases, we compute the CL fractions using a FDTD (Finite-Difference Time Domain) simulation, where a dipole source located at the center of the thin layer of interest represents the CL emission.

[Case 1] CdSe/ZnCdS QD layer (50 nm; $n = 1.7$) on CdTe absorber (3.5 µm; $n = 2.9$). The calculated CL fractions from the QD layer and the CdTe absorber are 5.2 % and 2.3 %, respectively.

[Case 2] CdSe/ZnCdS QD layer (1 µm; $n = 1.9$) on Si substrate (500 µm; $n = 3.95$). The simulated CL fraction from the QD layer is 7 % ± 2 %.

[Case 3] A Cu/Au (2 nm/7nm; $n = 0.2$) contact metal is located between the thin QD layer ($n = 1.7$) and the CdTe absorber ($n = 2.9$). The calculated CL fraction from the QD layer and the CdTe absorber is 1.9 % and 16 % ± 2 %, respectively.

Figure S-8. (a) Fractional CL emission to vacuum from an incoherent, unpolarized dipole source. Examples include (1) CdSe/ZnCdS QD layer (50 nm) on CdTe absorber (3.5 µm) (2) CdSe/ZnCdS QD layer (1 µm) on Si substrate (500 µm). (b) A thin metal layer (orange/yellow color) is located at the interface of the two mediums, such as a Cu/Au (2 nm/7nm) contact metal between the thin QD layer $\left(n_2 = 1.7 \right)$ and the CdTe absorber $\left(n_2 = 2.9 \right)$.

6. CL intensity and internal quantum efficiency

CL spectra were collected on various samples and compared with that of CdSe/ZnCdS quantum dots. The samples includes single crystalline bulk semiconductors (GaAs, InP, CdS), colloidal core/shell quantum dots (CdSe/CdS, CdSe/ZnS), and commercial phosphor powder ($SrAl_2O_4$).

The overall CL energy efficiency is given by:

$$\eta = \frac{(1-r)[hv]}{\beta E_g} \cdot IQE_{CL} \cdot \eta_t \cdot \eta_{esc}$$

where r is the backscattering coefficient, $[hv]$ is the mean photon energy, βE_g is the energy needed to generate thermalized electron-hole pairs, η_t is the transfer efficiency of electron-hole pairs to emission centers, IQE_{CL} is the internal quantum efficiency, and η_{esc} is the probability of escape of the generated photons. Commercial phosphors and direct band-gap semiconductors would generally have high transfer efficiency ($\eta_t \approx 1$). η_{esc} is proportional to the CL fraction (f_{CL}) that was estimated using the Eq. (S-4). Backscattered energy loss is associated with the primary electrons that leave the sample surface after one or several elastic or inelastic collisions. This loss depends on the atomic numbers or composition of the materials[10]. The remaining electron energy deposited in the sample participates in the ionization events. Earlier experiments showed that the generation of one electron-hole pair corresponds to the loss of incident electron energy $\beta \times E_g$, where E_g is the energy band-gap of the material with $\beta \approx 3$ for many inorganic semiconductors and insulators[12] [13]. The backscattered coefficient of each material was obtained from Monte Carlo simulations. Table 1 summarizes the calculated maximum energy efficiency ($hv / \beta E_g$).

The cathodoluminescence internal quantum efficiency (IQE_{CL}) is defined by the number of photons divided by the number of excited electron-hole pairs. Earlier experiments showed that

for many inorganic semiconductors and insulators the generation of one electron-hole pair corresponds to the loss of incident electron energy $\approx 3 \times E_g$, where E_g is the energy band-gap of the material[12]. The internal quantum efficiency of the high-purity, direct band-gap semiconductors (GaAs, InP) is expected to be >90 %. A well-known strontium aluminate phosphor ($SrAl_2O_4$; E_g = 6.5 eV) has a reported quantum efficiency > 95 %, emitting at $\approx$520 nm characteristic of the rare earth dopant[31].

Commercial colloidal core/shell QDs of CdSe/CdS (QD1) and CdSe/ZnS (QD2) capped with hexadecylamines were dispersed in hexane and toluene, respectively. Each QD film (> 1 um) was prepared by a drop-casting method onto a highly doped bare Si substrate (<0.005 ohm·cm) to reduce charging effects. To assemble a highly-packed QD layer, a small piece of Si substrate (1 cm × 3 cm) was inclined on a wedge and the QD solution was dropped at the bottom of the substrate. Following the slow-dry of the QD solvent, another drop casting was performed on top of the QD layer. A spectroscopic ellipsometry was performed on the thick part of the QD film, where the CL spectra were collected. Commercial bulk wafers ($\approx$400 μm thick) of GaAs, InP, and CdS were cleaned with acetone and isopropanol, and blown dry.

Each sample was mounted on an aluminum sample holder using a carbon tape and placed under the parabolic CL mirror. The z-height (step size of 50 μm) was optimized by maximizing CL counts in the spectrum. At this focal point, the CL photons are collected and collimated effectively to the spectrometer. The entrance slit to the spectrometer was wide open (1 mm) to maximize the collection of the CL photons, resulting in a broadening of the emission peaks but not affecting the integral count.

Figure S-9 displays the measured CL spectra at 10 keV. The characteristic peak at each CL spectrum is matching to the corresponding band-gaps, indicating band-edge recombination.

The high CL intensities of the CdSe/ZnCdS QD film, phosphor powder, and high-purity GaAs and InP were observed at different acceleration voltages as well. The total number of collected CL photons was obtained by integrating each spectrum. Due to the refractive indices of the materials, the fraction of the escaping photons from the materials to the vacuum is different. The normalized CL counts were calculated by dividing the total count by the CL fraction (see Table S-1). This normalization is accurate only for samples with flat surface, and the escape fraction is larger and displays strong variations in phosphors particles. Therefore, IQE is not calculated for phosphor sample. Figure S-9 shows the normalized CL counts at different acceleration voltages, indicating that the generated CL photons in the QD layer is similar to those in the high purity GaAs or InP.

Table S-1. Estimated maximum energy efficiency and fraction of CL emission

	E_g (eV)	λ (nm)[1]	Est. max. η (%)[2]	n [3]	Est. f_{CL} (%)[4]	Est. r [5]	Est. BSE (%)[5]	Relative IQE (%)[6]
QD1	2.0	635	33	1.9	7	0.38	28	7 ± 1
QD2	2.3	526	33	1.9	7	0.38	28	38 ± 7
CdS	2.4	516	33	2.4	3.8	0.37	27	16 ± 1
GaAs	1.45	850	33	3.7	1.2	0.32	22	98 ± 4
InP	1.35	920	33	3.3	1.7	0.37	27	100 ± 6
Phosphor	6.5	520	12	1.7	8.9	0.22	15	N/A
CdSe/ZnCdS (drop casting)	2	620	33	1.9	7	0.38	28	102 ± 7

*1. Peak wavelength extracted from the CL spectrum of each sample.

*2. max $\eta = \dfrac{hv}{\beta E_g} = \dfrac{hc}{3E_g\lambda}$, assumed that the backscatter coefficient (r) is 1 for all samples. h is

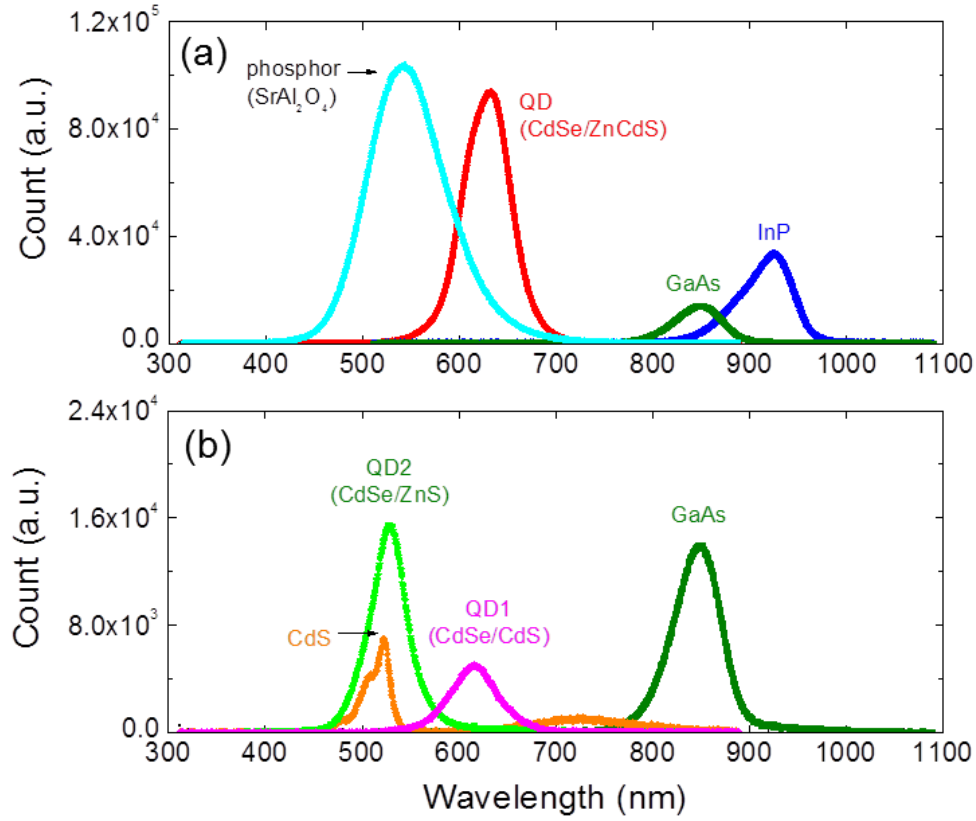Planck's constant, c is the speed of light in vacuum, and λ is the wavelength of photon.

*3. Refractive index obtained from spectroscopic ellipsometer measurements except QD1, QD2 (assumed the same value of CdSe/ZnCdS), and phosphor powder.

*4. Estimated CL fraction (f_{CL}) using the Eq. (S-4). The probability of escape of the generated photons (η_{esc}) is proportional to the CL fraction.

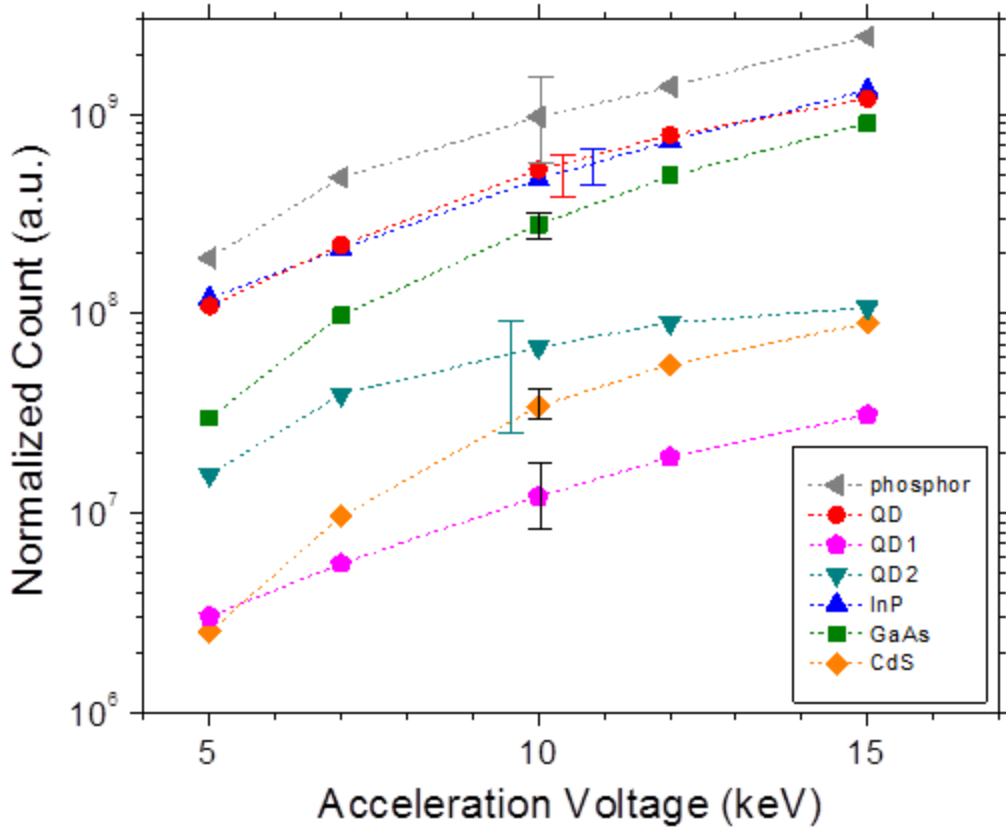*5. The backscattering coefficient (r) and the backscattered energy loss (BSE) of each material were calculated using Monte Carlo simulations. The total number of primary electrons in each simulation was 100,000. An insignificant variation of the backscattered coefficient and the energy loss at different acceleration voltages (<20 keV) was observed.

*6. $\dfrac{\Sigma E_{CL}}{\text{e-beam energy}} \approx (1-r)\left(\max \eta\right)\left(\eta_t = 1\right)\left(\eta_{IQE}\right)\left(f_{CL}\right); \ \left(\max \eta\right) = \dfrac{[hv]}{\b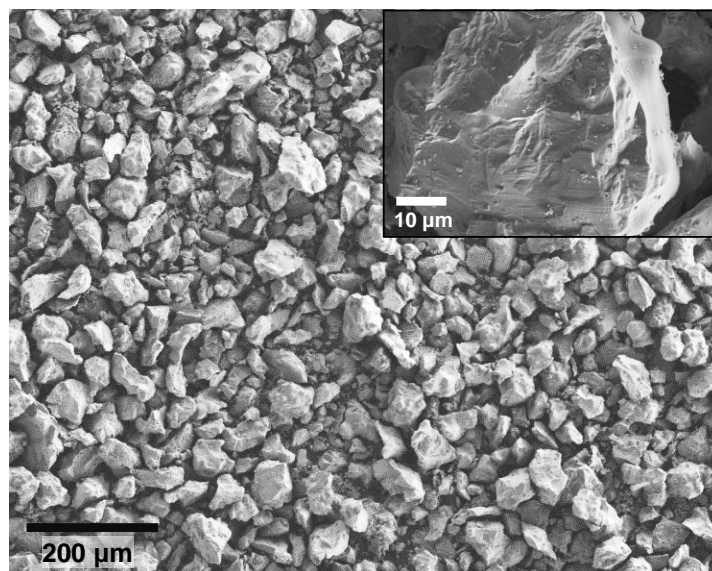eta E_g}$. $[hv]$ is the mean photon energy, βE_g is the energy needed to generate thermalized electron-hole pairs, r is the backscattering coefficient, η_t is the transfer efficiency of electron-hole pairs to emission centers, η_{IQE} is the internal quantum efficiency, and f_{CL} is CL fraction.

Figure S-9. (a) 10 keV CL spectra of CdSe/ZnCdS quantum dot film, phosphor $(Sr_{0.95}Eu_{0.02}Dy_{0.03}Al_2O_4)$, and GaAs and InP single crystalline materials. The characteristic peaks at 620 nm for QD, 850 nm for GaAs, and 920 nm for InP correspond to the band-edge recombination. A higher intensity and narrower peak is observed with CdSe/ZnCdS quantum dots. (b) 10 keV CL spectra of quantum dot films of QD1 (CdSe/CdS) and QD2 (CdSe/ZnS) and CdS single crystalline substrate compared to that of GaAs in (a).

Figure S-10. Total number of CL photons collected for 1s at different acceleration voltages $\left(\Sigma(\text{CL photons}) \approx (1-r)(\max \eta)(\eta_t = 1)(\eta_{IQE})(f_{CL})\right)$. The values were normalized by taking into account the CL fraction, the backscattered energy loss, and the number of generated photons for each material. The electron beam current increases proportionally with acceleration voltage (239 pA at 5keV, 266 pA at 7 keV, 329 pA at 10 keV, 364 pA at 12 keV, and 422 pA at 15 keV). Representative error bars indicate one standard deviation uncertainties due to the spectroscopic collection setup and background signal of the CCD (charged coupled device) detector. The larger standard deviation for the phosphor and QD2 compared to other materials is likely due to surface roughness. Figure S-11 shows a representative SEM image of the phosphor.

Figure S-11. An SEM image of phosphor powder ($SrAl_2O_4$) on a carbon adhesive tape that was used for cathodoluminescence (CL) measurements. The CL spectra were obtained by rastering an electron beam (10 μm $\times$ 10 μm) on the single grain of the phosphor shown in the inset. The standard deviation of the CL counts was calculated using 30 spectra on different grains.